ACS APPLIED MATERIALS & INTERFACES

Research Article

www.acsami.org

Interfacial Interactions of Semiconductor with Graphene and Reduced Graphene Oxide: CeO_2 as a Case Study

Liang Xu, Wei-Qing Huang,* Ling-Ling Wang, and Gui-Fang Huang*

Department of Applied Physics, Key Laboratory for Micro-Nano Physics and Technology of Hunan Province, Hunan University, Changsha 410082, China

Supporting Information

ABSTRACT: The pursuit of superb building blocks of light harvesting systems has stimulated increasing efforts to develop graphene (GR)-based semiconductor composites for solar cells and photocatalysts. One critical issue for GR-based composites is understanding the interaction between their components, a problem that remains unresolved after intense experimental investigation. Here, we use cerium dioxide (CeO_2) as a model semiconductor to systematically explore the interaction of semiconductor with GR and reduced graphene oxide (RGO) with large-scale ab initio calculations. The amount of charge transferred at the interfaces increases with the concentration of O atoms, demonstrating that the interaction between CeO_2 and RGO is much stronger than that between CeO_2 and GR due to the decrease of the average equilibrium distance between the interfaces. The stronger interaction between semiconductor and RGO is expected to be general, as evidenced by the results of two paradigms of TiO_2 and Ag_3PO_4 coupled with RGO. The interfacial interaction can tune the band structure: the $CeO_2(111)$/GR interface is a type-I heterojunction, while a type-II staggered band alignment exists between the $CeO_2(111)$ surface and RGO. The smaller band gap, type-II heterojunction, and negatively charged O atoms on the RGO as active sites are responsible for the enhanced photoactivity of CeO_2/RGO composite. These findings can rationalize the available experimental reports and enrich our understanding of the interaction of GR-based composites for developing high-performance photocatalysts and solar cells.

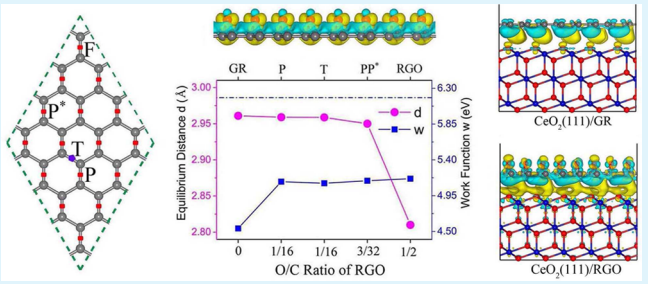

KEYWORDS: *interfacial interaction, electronic structure, graphene and reduced graphene oxide, semiconductor, photocatalytic properties, density functional theory*

1. INTRODUCTION

Understanding mechanisms and modifying photocatalytic performance have always been a prime interest of photocatalytic technologies. To develop novel photocatalysts, it is important to improve their visible light photocatalytic activity and structural stability during photocatalytic processes. Graphene (GR)-based semiconductor photocatalysts have recently attracted increasing attention for their promising potential for converting solar energy to chemical energy.[1−5] A group of GR-semiconductor nanocomposites, such as TiO_2/GR,[6,7] ZnS/GR,[8] ZnO/GR,[9,10] Ag_3PO_4/GR,[11] C_3N_4/GR,[12] CdS/GR,[13,14] MoS_2/GR,[8,15] SnS_2/GR,[16] and SnO_2/GR,[17,18] have been investigated experimentally. It has been demonstrated that two-dimensional (2D) GR can not only serve as a support material to which semiconductor particles anchor, but also greatly improve the photocatalytic performance of nanocomposites. For examples, TiO_2/GR nanocomposites exhibit much higher photocatalytic activity than bare TiO_2 for selective photoreduction of CO_2 to CH_4 under both UV and visible (vis) light irradiation.[7] CdS/GR composites have a high H_2 production rate of 1.12 mmol h^{-1} (about 4.87 times higher than that of pure CdS nanoparticles) under visible-light irradiation and an apparent quantum efficiency (QE) of 22.5% at wavelength of 420 nm.[13] Concurrently, nanocomposites of graphene oxide (GO) or reduced graphene oxide (RGO) and semiconductors are found to be high-performance photocatalysts (including TiO_2/RGO,[19] ZnO/GO,[20] Ag_3PO_4/GO,[21,22] C_3N_4/GO,[23] CuS/GO,[24] SnS_2/GO,[25] SnO_2/RGO,[17] $ZnIn_2S_4$/RGO,[26] and $BiVO_4$/RGO[27]). One typical case is that the MoS_2/RGO heterostructure shows significant photocatalytic activity toward the hydrogen evolution reaction in the wavelength range from the UV light through the near-infrared light.[28]

It is considered that the GR, GO, or RGO introduced into the nanocomposites mainly acts to promote the separation of charge carriers and transport of photogenerated electrons, which is responsible for the enhancement of photocatalytic performance. To explain the experimental results, GR, GO or RGO is generally assumed to be the electron shuttle to carry excited electrons from the semiconductors.[27,29] The first-principle calculations conducted by Gao[30] provide a theoretical support: there is a significant charge transfer from anatase

Received: August 30, 2014
Accepted: October 14, 2014
Published: October 14, 2014

TiO_2(001) plane to the GR at the ground electronic state. Using large-scale ab initio calculations, however, Du et al. reveals that the function of GR is to sensitize TiO_2,[31] supported by another theoretical study.[32] Other theoretical studies available to date on GR-semiconductor or carbon-semiconductor composites, including TiO_2/carbon nanotube,[33] TiO_2/fullerene,[34] and Ag_3PO_4/GR,[35] found that the charges always transfer to semiconductors. In ZnO/GR, the charge transfer direction depends on the kind of outermost layer atom in ZnO.[36,37] The calculated band gaps of these GR-semiconductor composites are much smaller than those obtained by experiments. Further investigations are thus necessary to settle these discrepancies. Moreover, the underlying mechanisms of the improved photocatalytic performance of GO (RGO)-semiconductors have not been revealed so far.

In this work, the interaction of semiconductor with GR and RGO is systematically explored via a model semiconductor of CeO_2. The choice of CeO_2 is motivated by its important industrial applications (e.g., in automotive catalytic converters to decrease pollutants from combustion exhausts[38]) and technological applications by virtue of its unique electronic properties. Furthermore, CeO_2 is believed to be one of the key materials for future hydrogen production technology, in particular for the water−gas-shift reaction and the conversion of ethanol and ethanol−water mixtures into dihydrogen.[39] More importantly, there are many experimental investigations on CeO_2/GR[40−48] and CeO_2/RGO,[49−52] whereas few theoretical studies are reported. Our results show that the charges transfer from GR (RGO) to CeO_2 due to the difference of their work functions. The amount of charge transferred is proportional to the concentration of O atoms absorbed on a RGO sheet. Thus, the interaction between CeO_2 and RGO is much stronger than that between CeO_2 and GR, and weakens as the concentration of O atom on the RGO sheet decreases. The interaction variation can be attributed to the change of the average equilibrium distance between the interfaces. The stronger interaction between semiconductor and RGO is expected to be general, as evidenced by the results of two paradigms of TiO_2 and Ag_3PO_4 coupled with GR and RGO. The change of band structures with the interaction can rationalize the UV−vis spectra and photocatalytic properties obtained by experiments.

2. COMPUTATIONAL DETAILS

Our density-functional theory (DFT) calculations are performed by using the Vienna ab initio simulation package (VASP)[53,54] based on DFT with the projector augmented wave (PAW) method.[55] Local density approximation (LDA)[56] is adopted because long-range van der Waals (vdW) interactions are expected to be significant in the systems. However, LDA has been generally known to underestimate the band gap of semiconductor, resulting into an overestimate for photoinduced electron transfer in photocatalytic processes. To get the correct band gap, all of the theoretical calculations are performed using the DFT/LDA+U method. We performed extensive tests to determine the appropriate U parameters, which reproduced the correct energy gap (3.2 eV) for cubic CeO_2. The appropriate Hubbard U values for Ce 4f and O 2p are 9.0 and 4.5 eV, respectively. The kinetic energy cutoff is 500 eV for the plane wave basis. Brillouin zone integrations are used on grids of 3 × 3 × 1 and 5 × 5 × 1 Monkhorst−Pack k-points[57] for geometry optimization and calculating the density of states, respectively. The symmetry unrestricted optimizations for geometry are performed by using the conjugate gradient scheme until the Hellman−Feynman force is smaller than 0.01 eV/Å. The vacuum space perpendicular to the CeO_2(111) surface is around 15 Å, which is enough to separate the interaction between periodic images.

It should be pointed out that (semi)local exchange-correlation functionals employed in standard DFT calculations lead to unphysical delocalization of lone pairs from the oxygen atoms in oxygen-terminated zigzag GR nanoribbons due to self-interaction errors.[58] Fortunately, the systems investigated here do not contain electron lone pairs. On the other hand, the quantitative prediction for the chemical and physical properties of CeO_2 requires an accurate description of the f states. Several groups have compared the results obtained by different DFT methods,[59−61] including the local spin density (LSDA), LDA+U, generalized gradient (GGA) approximations, Perdew−Burke−Ernzerhof (PBE0), and Heyd−-Scuseria−Ernzerhof (HSE) hybrid functionals. The calculated structural parameters, band gap, and the levels in the vicinity to Fermi level obtained from LDA+U, PBE0, and HSE06 are in agreement with each other and coincided with experimental results. Considering the very large system here (more than 400 atoms), we choose the DFT/LDA+U method. It is worth noting that using the chosen Hubbard U values, we can reproduce the correct lattice parameters and energy gap (3.2 eV) for cubic CeO_2 (Figure S1 Supporting Information). Moreover, the position and width of the Ce 4f and O 2p bands are in good agreement with the experiment and previous calculations. This indicates that the DFT/LDA+U computations can correctly characterize the Ce 4f and O 2p states. For comparison, we also calculate the electronic structure of a small model using the HSE06 method, which gives the same conclusion as those from the LDA+U method.

3. RESULTS AND DISCUSSION

The CeO_2/GR composite is first investigated. To construct the periodic interface, we choose a very large (5 × 5) stoichiometric cubic CeO_2(111) surface slab (nine layers) containing 150 O atoms and 75 Ce atoms, among which the three bottom layers are fixed at the bulk position, matching an (8 × 8) GR sheet (128 C atoms), as shown in Figure 1a,b. This gives rise to minor compressed deformation of GR, resulting into a 2.8% lattice mismatch. The calculated equilibrium distance between the GR sheet and the top of CeO_2(111) surface is 2.96 Å, which is in consistent with those in other GR-semiconductor composites.[30,37] After optimization, the GR

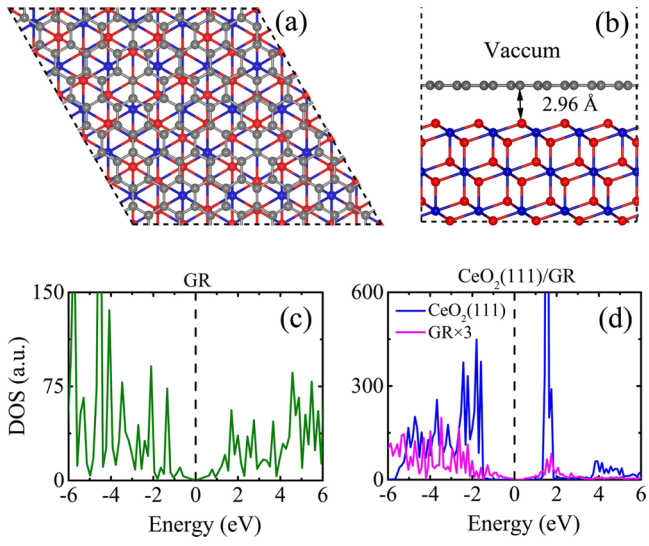

Figure 1. (a) Top and (b) side view of the simulated interface between GR and the cubic CeO_2(111) surface model. Gray, red, and purple spheres represent C, O, and Ce atoms, respectively. DOS for an (c) isolated GR sheet and (d) CeO_2(111)/GR composite (the magenta and blue lines are for GR and CeO_2(111), respectively). The DOS of GR in the CeO_2(111)/GR composite is amplified 3 times for the eyes. The Fermi level is set to zero.

sheet is quite flat, indicating that the $CeO_2(111)$/GR interaction is indeed vdW rather than covalent, in accordance with previous studies.[35,37]

To explore the interaction between CeO_2 and GR, we have calculated the density of states (DOSs) of individual CeO_2 and GR sheet before and after the formation of the hybrid interface, as shown in Figure 1c,d. The calculated band gap (between the occupied 2p band of O and unoccupied empty 4f band of Ce) of pure CeO_2 is 3.2 eV, which is in agreement with the well-established experimental value (Figure S1, Supporting Information). Figure 1c shows that the monolayer graphene sheet is a zero-gap semiconductor; therefore, GR cannot be used directly in many applications such as photocatalysis and field-effect transistors. Upon the formation of a hybrid interface, the band gap of $CeO_2(111)$/GR is about 0.48 eV. The interaction between CeO_2 and GR induces a band gap opening right at the Dirac point of GR, and the Fermi level is up-shifted by around 1.5 eV relative to the VBM of $CeO_2(111)$ surface (Figure 1d). However, their interaction is not strong enough to effectively change the electronic structure of the $CeO_2(111)$ surface in the absence of covalent bonding. Compared to the pure $CeO_2(111)$ surface (Figure S1b, Supporting Information), the band gap (3.15 eV) of $CeO_2(111)$ in CeO_2/GR hybrid has only slight variation. The weak coupling can further confirmed by Bader charge analysis, which shows that a small charge transfer of only 0.001 *e* per C atom from GR to the $CeO_2(111)$ surface.

Closer inspection to Figure 1d reveals that the band edges of GR nest into the band gap region of CeO_2. In photocatalysis, such band alignment is not beneficial for the separation of photogenerated electron−hole pairs. When the incident light illuminates on the CeO_2, electrons are excited to the conduction band (CB) and subsequently transferred to the CB minimum (CBM) of GR. Meanwhile, the photogenerated holes transfer to GR as well due to the lower valence band maximum (VBM) of CeO_2. As a result, the photogenerated charge carriers do not separate at the interface but recombine readily on the GR sheet. Therefore, the GR might act as recombination centers and degrade the photocatalytic activities of CeO_2/GR composite. The results can reasonably expound the experimental reports that the CeO_2/GR composites have various superior performances (e.g., supercapacitor performance,[41] higher photoluminescence efficiency,[43] and the anode material for lithium ion battery[40,48]), rather than photocatalytic properties.

Recent experiments have demonstrated that the CeO_2/RGO composites display much higher catalytic activity than pure CeO_2.[46,49,62,63] To uncover the mechanism, the electronic structures of CeO_2/RGO composites are studied. We first consider RGO with C/O atomic ratio of 2. The $CeO_2(111)$/RGO composite can be obtained by fully adsorbing the O atom on the two parallel edges (P and P* in Figure 2a) of honeycomb lattice in $CeO_2(111)$/GR (Figure 2a,b). The whole system contains 417 atoms with 2696 valence electrons. After the geometry optimizations, the flat C atom layer suggests that the $CeO_2(111)$/RGO interaction is also vdW rather than covalent. The equilibrium distance (2.81 Å) between RGO and the top of $CeO_2(111)$ surface is smaller than that of CeO_2/GR, indicating that the interaction between RGO and CeO_2 becomes stronger. The stronger interfacial adhesion of CeO_2/RGO is also reflected by more charge transfer: Bader charge analysis shows that 0.36 *e* per C atom transfers from RGO to the CeO_2 and O atom in RGO.

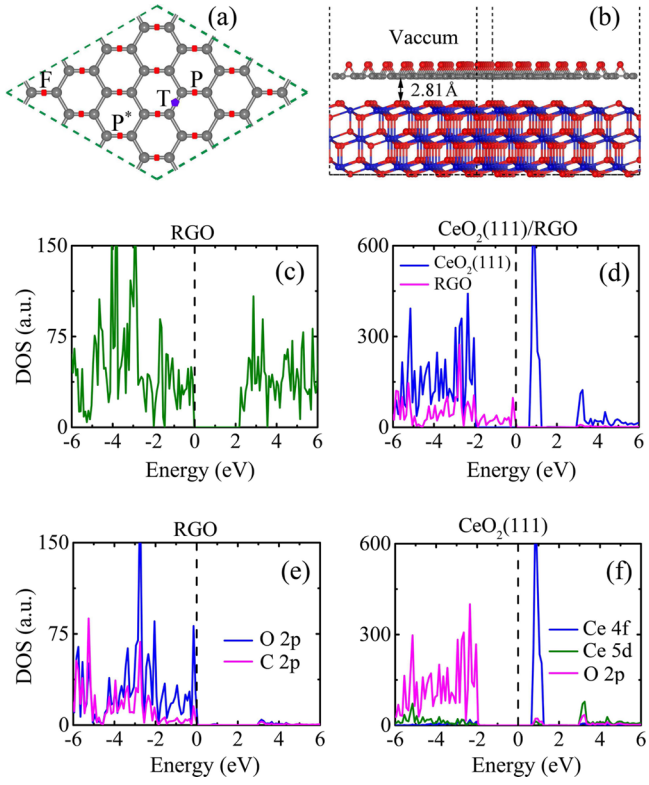

Figure 2. (a) Top view of one-quarter of the calculated RGO cell. Selected adsorption positions for the second O atom with respect to the first fixed O atom (F), are indicated by P, T, and P* in RGO. (b) Side view of the simulated interface between the $CeO_2(111)$ surface and the RGO (O/C = 1/2) model. Gray, red, and purple spheres represent C, O, and Ce atoms, respectively. DOS for an (c) isolated RGO sheet and (d) $CeO_2(111)$/RGO composite (the magenta and blue lines are for GR and $CeO_2(111)$, respectively). DOS for individual species for the (e) RGO and (f) $CeO_2(111)$. The vertical dashed lines indicate the Fermi level.

The discrepancy of interactions in CeO_2/GR and CeO_2/RGO can be visualized (Figure 3a,b) by three-dimensional charge density difference of $\Delta\rho = \rho_{CeO_2(111)/GR(RGO)} - \rho_{CeO_2(111)}$

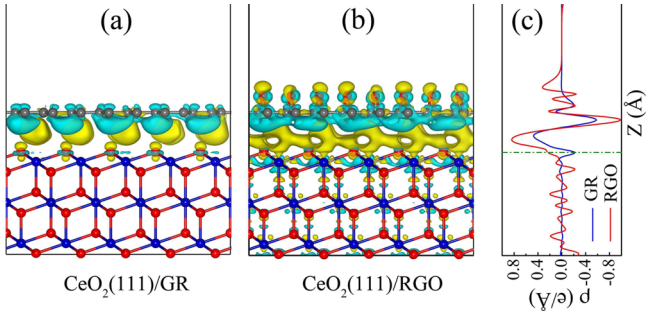

Figure 3. 3D Charge density differences for (a) $CeO_2(111)$/GR composite and (b) $CeO_2(111)$/RGO (O/C = 1/2) composite. The yellow and cyan regions represent charge accumulation and depletion, respectively; the isosurface value is 0.0006 *e*/Å^3. (c) Planar averaged charge density difference for (blue) the $CeO_2(111)$/GR composite and (green) the $CeO_2(111)$/RGO composite as a function of position in the *z*-direction. The horizontal dashed line indicates the location of the top layer of the $CeO_2(111)$ surface. The plots show that charge transfer occurs significantly between the $CeO_2(111)$/RGO composite over that of $CeO_2(111)$/GR composite.

dx.doi.org/10.1021/am5058772 | ACS Appl. Mater. Interfaces 2014, 6, 20350−20357

$-\rho_{GR(RGO)}$, where $\rho_{CeO_2(111)/GR(RGO)}$, $\rho_{CeO_2(111)}$, and $\rho_{GR(RGO)}$ are the charge densities of the composite, $CeO_2(111)$ surface, and free-standing GR(RGO) in the same configuration, respectively. Figure 3a renders that charge redistribution mostly occurs at the CeO_2/GR interface region, while there is almost no charge transfer to the CeO_2 farther from the interface. In contrast, for the CeO_2/RGO interface, charge redistribution takes place in the whole RGO and several atomic layers in CeO_2 besides the interface due to a strong donor−acceptor interaction, leading to a large amount of charge transferred. The plot also directly reflects the hybridization between the in-plane p_{xy} orbital of O atom and the out-of-plane p_z frontier orbital of GR. Figure 3c displays the planar averaged charge density difference along the direction perpendicular to the $CeO_2(111)$ surface, which can provide quantitative results of charge transfer and redistribution. The horizontal dashed line is the position of the top layer of the CeO_2 surface. The positive values denote electron accumulation, and negative values represent electron depletion. This plot further confirms that efficient charge transfer occurs in both cases, despite the fact that the transferred charge amount in the CeO_2/RGO interface is much greater than that in the CeO_2/GR interface.

To gain insight into the origin of enhanced photocatalytic activity of CeO_2/RGO composites, we present the DOSs of individual CeO_2 and RGO sheet before and after formation of the hybrid interface in Figure 2c,d. The RGO layer has a wide band gap of 2.28 eV, while the band gap of CeO_2/RGO is small (0.65 eV). Such a small band gap would lead to the absorption in the entire visible spectrum, and even in the infrared region, and thus enhance photocatalytic activity. Most importantly, Figure 2d indicates that different from the CeO_2/GR interface, the CeO_2/RGO interface becomes a type II heterojunction, namely, with both the valence and conduction band edges of CeO_2 below the corresponding RGO counterparts, which greatly facilitates effective separation of carriers. This is similar to the anatase−rutile TiO_2 composite.[64] With light illumination, the electrons at the top valence band (C and O 2p states in RGO, Figure 2e) are excited to the CB consisting of Ce 4f states with small O 2p states mixing (Figure 2f), that is, photogenerated electrons transfer from RGO to CeO_2, leading to electron−hole pair separation. Moreover, the negatively charged O atoms on the RGO (Figure 3b) are active sites for photocatalysis. It can therefore be concluded that the smaller band gap, the formation of type-II heterojunction, and the negatively charged O atoms on the RGO are responsible for the enhancement of photocatalytic activity of CeO_2/RGO photocatalyst.

The interaction of CeO_2 and RGO with an O/C atomic ratio less than 1/2 can be demonstrated by using three typical structures: CeO_2/RGO−P, CeO_2/RGO−T, and CeO_2/RGO−PP*. As one O atom is fixed at F, the other O atom is adsorbed on position P(T) (Figure 2a). The RGO with an O/C ratio of 1/16 is denoted as RGO−P (RGO−T). The RGO−PP* (i.e., the other two O atoms adsorbed on positions P and P* besides the fixed O atom at F) has a O/C ratio of 3/16. Figure 4 illustrates the DOSs of individual RGO sheet and CeO_2 before and after formation of the hybrid interface. The calculated band gaps of RGO−P, RGO−T, and RGO−PP* are 1.1, 0.29, and 0.96 eV, respectively. Interestingly, upon formation of an interface, the band gaps of the corresponding composites become 1.1, 0.31, and 0.51 eV, respectively. This indicates that the concentration or position of the O atom in RGO can tune

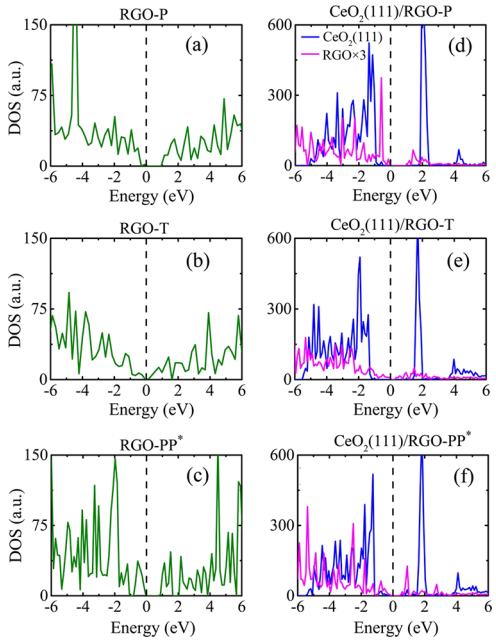

Figure 4. DOS for (a) RGO−P sheet, (b) RGO−T sheet, (c) RGO−PP* sheet, (d) $CeO_2(111)$/RGO−P composite, (e) $CeO_2(111)$/RGO−T composite, and (f) $CeO_2(111)$/RGO−PP* composite. The DOSs of the isolated sheets are presented in green lines, and those of individual RGO (O/C < 1/2) and $CeO_2(111)$ are plotted in magenta and blue lines, respectively. The vertical dashed lines indicate the Fermi level.

the band structure of CeO_2/RGO, that is, interaction between CeO_2 and RGO.

The analysis of the charge transfer following the formation of the CeO_2/RGO interface (Figure S2, Supporting Information) reveals that once O atom is adsorbed on GR to form RGO, the interaction between them will be reinforced. Moreover, the amount of efficient charge transfer in the CeO_2/RGO interface increases as the concentration of O atoms in RGO rises (Figure S2c, Supporting Information). The band alignment of CeO_2/RGO interfaces (the three lower panels of Figure 4) suggests that the CeO_2/RGO−PP* composite is the most appropriate photocatalyst due to its small band gap and the orbital hybridization between CeO_2 and RGO in the vicinity of Fermi level.

The experimentally measured UV−vis spectra of CeO_2/RGO nanocomposites[47,50,62,63] show the absorption edges at 400 nm, corresponding to the optical band gap of 3.10 eV. A close analysis to Figure 4 sheds a brilliant light on these roughly identical results. Just like the DOS of CeO_2/RG, the band edges of RGO also nest into the band gap region of CeO_2 (Figure 4). The band gap of $CeO_2(111)$ surface coupled to RGO is about 2.90 eV, and some intermediated levels appear in the band gap of the CeO_2/RGO−P and CeO_2/RGO−PP* systems. Because the states in the bottom of the CB and the top of the VB from the RGO are quite low (see the lower panels of Figure 4), the values of corresponding matrix elements in equation of the imaginary part of the dielectric function are very small, which results in very weak optical absorption in the visible-light region. Therefore, the intrinsic band gap of CeO_2 in CeO_2/RGO systems has a slight change, indicating that the electron transition from O 2p at the VB to Ce 4f at the CB is the dominant process under UV−vis irradiation, leading to a slight red-shift of the absorption edges (Figure S3, Supporting

Information). In most experiments, the GR (RGO, GO) in the semiconductor composites is obtained using natural flake graphite, rather than exfoliated graphite, as a starting material by thermal, chemical, or electrochemical treatments. Naturally, the GR-based semiconductor composites have a mixed distribution of GR, GO, and RGO with various C/O ratios. Therefore, the measured UV−vis spectra of CeO_2/GR(RGO) nanocomposites are the superimposition of those of CeO_2/GR, CeO_2/GO, and CeO_2/RGO. This can expound the UV−vis spectra difference between model calculations and experiments.

The charge transfer at the GR-semiconductor interfaces is generally rationalized in terms of the difference in their work functions.[31−34,41] To understand the origin of different charge transfer in the interfaces discussed above, the work functions for the CeO_2(111) surface, GR, RGO, RGO−P, RGO−T, and RGO−PP* layers have been calculated by aligning the Fermi level relative to the vacuum energy level, as shown in Figure 5b.

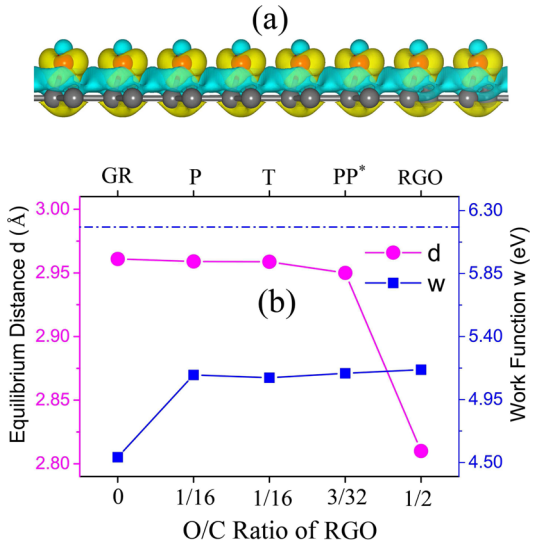

Figure 5. (a) Three-dimensional charge density differences for a RGO (O/C = 1/2) sheet. (b) Variations in average distance between RGO(GR) and CeO_2(111) surface and the work function of system with different C/O ratios in RGO. The horizontal dashed line indicates the work function of the CeO_2(111) surface.

The work function of the CeO_2(111) surface is 6.18 eV, larger than those of GR (RGO). Compared to that of RGO, the GR sheet has the smallest work function, i.e., 4.55 eV, in agreement with previous studies.[31,32,41] When O atom is adsorbed on GR, the work function increases: those of the RGO−P, RGO−T, RGO−PP*, and RGO layers are 5.12, 5.09, 5.13, and 5.18 eV, respectively, demonstrating that the concentration or position of O atom in RGO has little effect on its work function. Apparently, the difference of work functions between the CeO_2(111) surface and the GR layer is greater than that between the CeO_2(111) surface and the RGO layer. Thus, the spontaneous interfacial charge transfer from GR(RGO) to CeO_2 can be rationalized by the higher work function of the CeO_2(111) surface. But, the amount of charge transferred at the interface does not hinge on the difference of work functions.

The amount of charge transferred at the interface is the key factor for converting light energy into electricity or fuels, and its origin is still challenging. We have calculated the average distance, *d*, between the top of the CeO_2(111) surface and all of the carbon atoms, as displayed in Figure 5b. When the O/C ratio is smaller than 1/2, the carbon atom layer in RGO interfaced with CeO_2(111) surface is undulated, and the typical case is the CeO_2/RGO−P interface (Figure S4 a, Supporting Information). This is reasonable from the fact that even the suspended graphene sheets are not perfectly flat; as reported, "they exhibit intrinsic microscopic roughening such that the surface normal varies by several degrees and out-of-plane deformations reach 1 nm".[65] Figure 5 shows that the average distance, *d*, is 2.962 Å in the CeO_2/GR interface, decreases with the O/C ratio in the CeO_2/RGO interface, and finally reaches the smallest value of 2.81 Å as O/C = 1/2. The CeO_2/RGO−P and CeO_2/RGO−T interfaces with the identical O/C ratio of 1/16 have the same value of *d*. The change trend of *d* is opposite to that of the amount of charge transferred at the interface: the smaller average distance, *d*, the more amount of charge transferred. One can therefore conclude that the amount of charge transferred at the GR(RGO)-semiconductor interface depends on the average distance, *d*, between them, and the smaller average distance results in stronger interaction. The shorter average distance, *d*, can be attributed to the enhanced vdW force between CeO_2 and RGO, hence the charge distribution fluctuations of RGO sheet, as shown in Figure 5a.

In support of the given argument, we have recalculated all models discussed above by using a relative smaller supercell (a 2 × 2 CeO_2(111) surface interfaced with a 3 × 3 GR(RGO) sheet). The smaller model has a minor tensile deformation of GR just opposite the larger one, only leading to a 3.7% lattice mismatch. The conclusion made from these smaller models is fundamentally the same as that from the larger ones. As an example, the optimized interface structures of the CeO_2(111)/RGO interface and its total DOS and partial DOSs for RGO and CeO_2(111) surface are presented in Figure 6a−d. The total DOS of the CeO_2(111)/RGO interface and partial DOSs for RGO and CeO_2 show a band gap of 0.701 eV, and the top VB is dominated by C and O 2p states in RGO, while the bottom CB is mainly composed of Ce 4f states mixed with some O 2p states. This is consistent with those in the larger model. Several studies[59−61] found that, compared to LDA and GGA methods, the hybrid HSE functional gives a more consistent picture of both the structural and electronic properties of CeO_2, and in particular, the latter can present the correct magnetic states, whereas the former cannot. It is therefore essential to prove the validity of the results from the LDA+U method. Because of the high computational cost of the hybrid computations, the smaller model of the CeO_2(111)/RGO interface is chosen for HSE06 calculation. The DOSs calculated by HSE06 are given in Figure 6e−g. The HSE06 and LDA+U functionals give similar, but not identical, descriptions of the CeO_2(111)/RGO composite. One can see that the HSE06 functionals present a larger band gap of 1.02 eV (Figure 6e), a wider lowest unoccupied 4f state (Figure 6g), and a greater energy difference between the lowest 4f state and 5d state of CeO_2, as well as a lager band gap of RGO (Figure 6f). These results are in agreement with those reported by Da Silva et al.[60] It is, however, very important for us to note that the components of the upper VB and the bottom CB of the CeO_2(111)/RGO composite are same for both LDA+U and HSE06 functionals. Therefore, the conclusion given above is reasonable and reliable, independent of computational methods.

The interaction between CeO_2 and RGO being stronger than that between CeO_2 and GR is expected to be general in GR-based semiconductor composites. TiO_2 and Ag_3PO_4, as two

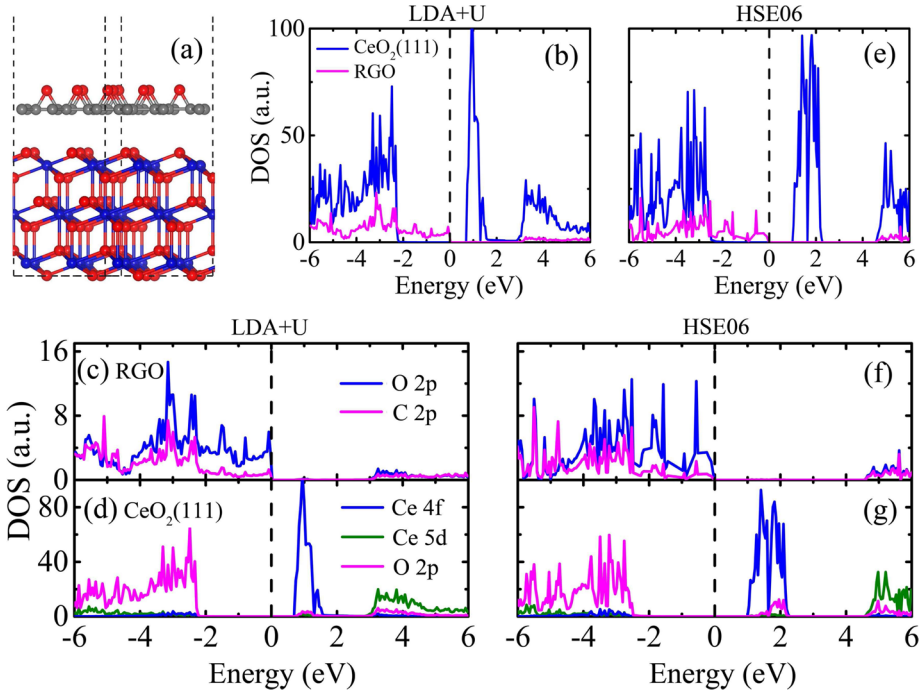

Figure 6. (a) Optimized interface structure: a (2 × 2) CeO_2(111) surface interfaced with a (3 × 3) RGO sheet; (b and e) calculated DOS of (red) RGO and (black) CeO_2(111) surface. Calculated PDOS of (c and f) RGO and (d and g) CeO_2(111) surface. The curves in (b, c, and d) are obtained by using LDA+U method, and those in (e, f, and g) are obtained by using HSE06 method. The vertical dashed lines indicate the Fermi level.

paradigms, are chosen to study the coupling between semiconductor photocatalyst and GR(RGO). For this kind of composite, the coupling strength can be reflected by the extent of charge transfer at the interfaces, that is, the more charge transfer, the stronger coupling is. Figure S5 (Supporting Information) shows that the amount of charge transferred at the TiO_2/RGO interface is much larger than that at the TiO_2/GR interface. This situation for the Ag_3PO_4/RGO composite is more pronounced compared to the Ag_3PO_4/GR interface (Figure S6, Supporting Information). The greater charge transfer indicates that the RGO layer shows stronger interaction with the surface of semiconductors. These results provide convincing evidence that the coupling strength between semiconductor and RGO is stronger than that between semiconductor and GR.

More recently, the interactions of semiconductor−semiconductor and semiconductor−metal photocatalysts are reviewed.[66] In the photocatalysis, the charge transfer is a dynamical process. It is therefore of great importance to study the mechanisms on charge separation and energy losses in composite, particularly in the GR-based composites in which charge separation competes with energy losses that can result in rapid electron−hole annihilation inside metallic GR.[67] Considerable effort has been devoted to the dynamical process of charge transfer in hybrid systems.[68,69] Thus, the excited-state calculations are needed to deeply reveal the interaction in the systems studied here, but they are as yet unreachable for such a large system with more than 400 atoms.

4. SUMMARY

In summary, the electronic structure and interfacial charge transfer have been investigated in hybrid CeO_2/GR(RGO) systems using large-scale density functional (both LDA+U and HSE06) calculations to explore the interfacial interaction in GR-based semiconductor composites. The CeO_2/GR composite can form a potentially excellent photovoltaic solar cell owing to a small interaction that leads to a slight charge transfer. In contrast, due to effective charge separation across the CeO_2/RGO interface, the RGO is better than the GR as a photosensitizer to induce greater enhancement of the visible light photoactivity. The interfacial interaction between CeO_2 and RGO is much stronger than that between CeO_2 and GR, and it is weakened as the concentration of O atoms on the RGO sheet decreases. The interaction increases as the average equilibrium distance between the interfaces decreases. The stronger interaction between semiconductor and RGO is expected to be general, which is further verified by the results of two paradigms of TiO_2 and Ag_3PO_4 coupled with RGO. The interaction at the interface can alter the band structures: The CeO_2(111)/GR interface is a type-I heterojunction, making it superior in various performances other than photocatalytic properties. On the contrary, a type-II staggered band alignment exists between the CeO_2(111) surface and RGO. The smaller band gap, type-II heterojunction, and the negatively charged O atoms on the RGO are responsible for the enhanced photoactivity of the CeO_2/RGO composite. This work can rationalize the available experimental results and enriches our understanding on the interaction of GR-based composites for developing high-performance photocatalysts and solar cells.

■ ASSOCIATED CONTENT

Supporting Information

Calculations of the band structure and (partial)DOS for pure CeO_2 and CeO_2(111) surface, plots of 3D charge density differences for CeO_2(111)/GR and CeO_2(111)/RGO−P nanocomposite, calculated imaginary part of the dielectric function and absorption spectra for the CeO_2(111) surface, CeO_2(111)/RGO−P, CeO_2(111)/RGO−PP*, and

CeO_2(111)/RGO (O/C = 1/2) nanocomposite, optimized CeO_2/RGO−P nanocomposite and plot of the longest and shortest distances between C atoms in RGO and top O atoms in CeO_2 as a function of O/C ratio, optimized nanocomposite of a (2 × 2) CeO_2(111) surface interfaced with a (3 × 3) RGO (O/C = 1/2) sheet and plot of the (partial)DOS of RGO and CeO_2(111), plots of 3D charge density differences for TiO_2(110)/GR, TiO_2(110)/RGO (O/C = 1/2), Ag_3PO_4(100)/GR and Ag_3PO_4(100)/RGO (O/C = 1/2) nanocomposite. This material is available free of charge via the Internet at http://pubs.acs.org.

AUTHOR INFORMATION

Corresponding Authors

*E-mail: wqhuang@hnu.edu.cn.
*E-mail: gfhuang@hnu.edu.cn.

Notes

The authors declare no competing financial interest.

ACKNOWLEDGMENTS

This work is supported by the Hunan Provincial Natural Science Foundation of China (Grant No. 12JJ3009), and the Changsha Science and Technology Plan Projects (k1403067-11).

REFERENCES

(1) Xiang, Q.; Yu, J. G.; Jaroniec, M. Graphene-Based Semiconductor Photocatalysts. *Chem. Soc. Rev.* **2012**, *41*, 782−796.

(2) Kamat, P. V. Quantum Dot Solar Cells. The Next Big Thing in Photovoltaics. *J. Phys. Chem. Lett.* **2013**, *4*, 908−918.

(3) Yeh, T.-F.; Cihlář, J.; Chang, C.-Y.; Cheng, C.; Teng, H. Roles of Graphene Oxide in Photocatalytic Water Splitting. *Mater. Today* **2013**, *16*, 78−84.

(4) Xie, G.; Zhang, K.; Guo, B.; Liu, Q.; Fang, L.; Gong, J. R. Graphene-Based Materials for Hydrogen Generation from Light-Driven Water Splitting. *Adv. Mater.* **2013**, *25*, 3820−3839.

(5) Xiang, Q.; Yu, J. G. Graphene-Based Photocatalysts for Hydrogen Generation. *J. Phys. Chem. Lett.* **2013**, *4*, 753−759.

(6) Huang, Q.; Tian, S.; Zeng, D.; Wang, X.; Song, W.; Li, Y.; Xiao, W.; Xie, C. Enhanced Photocatalytic Activity of Chemically Bonded TiO_2/Graphene Composites Based on the Effective Interfacial Charge Transfer through the C−Ti Bond. *ACS Catal.* **2013**, *3*, 1477−1485.

(7) Liang, Y. T.; Vijayan, B. K.; Lyandres, O.; Gray, K. A.; Hersam, M. C. Effect of Dimensionality on the Photocatalytic Behavior of Carbon−Titania Nanosheet Composites: Charge Transfer at Nanomaterial Interfaces. *J. Phys. Chem. Lett.* **2012**, *3*, 1760−1765.

(8) Xiang, Q.; Yu, J. G.; Jaroniec, M. Synergetic Effect of MoS_2 and Graphene as Cocatalysts for Enhanced Photocatalytic H_2 Production Activity of TiO_2 Nanoparticles. *J. Am. Chem. Soc.* **2012**, *134*, 6575−6578.

(9) Bai, X.; Wang, L.; Zong, R.; Lv, Y.; Sun, Y.; Zhu, Y. Performance Enhancement of ZnO Photocatalyst via Synergic Effect of Surface Oxygen Defect and Graphene Hybridization. *Langmuir* **2013**, *29*, 3097−3105.

(10) Joshi, B. N.; Yoon, H.; Na, S.-H.; Choi, J.-Y.; Yoon, S. S. Enhanced Photocatalytic Performance of Graphene−ZnO Nanoplatelet Composite Thin Films Prepared by Electrostatic Spray Deposition. *Ceram. Int.* **2014**, *40*, 3647−3654.

(11) Yang, X.; Cui, H.; Li, Y.; Qin, J.; Zhang, R.; Tang, H. Fabrication of Ag_3PO_4−Graphene Composites with Highly Efficient and Stable Visible Light Photocatalytic Performance. *ACS Catal.* **2013**, *3*, 363−369.

(12) Xiang, Q.; Yu, J. G.; Jaroniec, M. Preparation and Enhanced Visible-Light Photocatalytic H_2-Production Activity of Graphene/C_3N_4 Composites. *J. Phys. Chem. C* **2011**, *115*, 7355−7363.

(13) Li, Q.; Guo, B.; Yu, J. G.; Ran, J.; Zhang, B.; Yan, H.; Gong, J. R. Highly Efficient Visible-Light-Driven Photocatalytic Hydrogen Production of CdS-Cluster-Decorated Graphene Nanosheets. *J. Am. Chem. Soc.* **2011**, *133*, 10878−10884.

(14) Pan, S.; Liu, X. CdS-Graphene Nanocomposite: Synthesis, Adsorption Kinetics and High Photocatalytic Performance under Visible Light Irradiation. *New J. Chem.* **2012**, *36*, 1781−1787.

(15) Chang, K.; Mei, Z.; Wang, T.; Kang, Q.; Ouyang, S.; Ye, J. MoS_2/Graphene Cocatalyst for Efficient Photocatalytic H_2 Evolution under Visible Light Irradiation. *ACS Nano* **2014**, *8*, 7078−7087.

(16) Jiang, J.; Feng, Y.; Mahmood, N.; Liu, F.; Hou, Y. SnS_2/Graphene Composites: Excellent Anode Materials for Lithium Ion Battery and Photolysis Catalysts. *Sci. Adv. Mater.* **2013**, *5*, 1667−1675.

(17) Seema, H.; Kemp, K. C.; Chandra, V.; Kim, K. S. Graphene−SnO_2 Composites for Highly Efficient Photocatalytic Degradation of Methylene Blue under Sunlight. *Nanotechnology* **2012**, *23*, 355705.

(18) Zhuang, S.; Xu, X.; Feng, B.; Hu, J.; Pang, Y.; Zhou, G.; Tong, L.; Zhou, Y. Photogenerated Carriers Transfer in Dye-Graphene-SnO_2 Composites for Highly Efficient Visible-Light Photocatalysis. *ACS Appl. Mater. Interfaces* **2013**, *6*, 613−621.

(19) Wang, P.; Wang, J.; Ming, T.; Wang, X.; Yu, H.; Yu, J.; Wang, Y.; Lei, M. Dye-Sensitization-Induced Visible-Light Reduction of Graphene Oxide for the Enhanced TiO_2 Photocatalytic Performance. *ACS Appl. Mater. Interfaces* **2013**, *5*, 2924−2929.

(20) Liu, X.; Pan, L.; Zhao, Q.; Lv, T.; Zhu, G.; Chen, T.; Lu, T.; Sun, Z.; Sun, C. UV-Assisted Photocatalytic Synthesis of ZnO−Reduced Graphene Oxide Composites with Enhanced Photocatalytic Activity in Reduction of Cr(VI). *Chem. Eng. J.* **2012**, *183*, 238−243.

(21) Liu, L.; Liu, J.; Sun, D. D. Graphene Oxide Enwrapped Ag_3PO_4 Composite: Towards a Highly Efficient and Stable Visible-Light-Induced Photocatalyst for Water Purification. *Catal. Sci. Technol.* **2012**, *2*, 2525−2532.

(22) Liang, Q.; Shi, Y.; Ma, W.; Li, Z.; Yang, X. Enhanced Photocatalytic Activity and Structural Stability by Hybridizing Ag_3PO_4 Nanospheres with Graphene Oxide Sheets. *Phys. Chem. Chem. Phys.* **2012**, *14*, 15657−15665.

(23) Liao, G.; Chen, S.; Quan, X.; Yu, H.; Zhao, H. Graphene Oxide Modified gC_3N_4 Hybrid with Enhanced Photocatalytic Capability under Visible Light Irradiation. *J. Mater. Chem.* **2012**, *22*, 2721−2726.

(24) Zhang, Y.; Tian, J.; Li, H.; Wang, L.; Qin, X.; Asiri, A. M.; Al-Youbi, A. O.; Sun, X. Biomolecule-Assisted, Environmentally Friendly, One-Pot Synthesis of CuS/Reduced Graphene Oxide Nanocomposites with Enhanced Photocatalytic Performance. *Langmuir* **2012**, *28*, 12893−12900.

(25) An, X.; Jimmy, C. Y.; Tang, J. Biomolecule-Assisted Fabrication of Copper Doped SnS_2 Nanosheet-Reduced Graphene Oxide Junctions With Enhanced Visible-Light Photocatalytic Activity. *J. Mater. Chem. A* **2014**, *2*, 1000−1005.

(26) Ye, L.; Fu, J.; Xu, Z.; Yuan, R.; Li, Z. Facile One-Pot Solvothermal Method to Synthesize Sheet-on-Sheet Reduced Graphene Oxide (RGO)/$ZnIn_2S_4$ Nanocomposites with Superior Photocatalytic Performance. *ACS Appl. Mater. Interfaces* **2014**, *6*, 3483−3490.

(27) Ng, Y. H.; Iwase, A.; Kudo, A.; Amal, R. Reducing Graphene Oxide on a Visible-Light $BiVO_4$ Photocatalyst for an Enhanced Photoelectrochemical Water Splitting. *J. Phys. Chem. Lett.* **2010**, *1*, 2607−2612.

(28) Meng, F.; Li, J.; Cushing, S. K.; Zhi, M.; Wu, N. Solar Hydrogen Generation by Nanoscale p-n Junction of p-type Molybdenum Disulfide/n-type Nitrogen-Doped Reduced Graphene Oxide. *J. Am. Chem. Soc.* **2013**, *135*, 10286−10289.

(29) Zhang, Y.; Tang, Z.-R.; Fu, X.; Xu, Y.-J. TiO_2-Graphene Nanocomposites for Gas-Phase Photocatalytic Degradation of Volatile Aromatic Pollutant: Is TiO_2-Graphene Truly Different from Other TiO_2-Carbon Composite Materials? *ACS Nano* **2010**, *4*, 7303−7314.

(30) Gao, H.; Li, X.; Lv, J.; Liu, G. Interfacial Charge Transfer and Enhanced Photocatalytic Mechanisms for the Hybrid Graphene/Anatase TiO_2(001) Nanocomposites. *J. Phys. Chem. C* **2013**, *117*, 16022−16027.

(31) Du, A.; Ng, Y. H.; Bell, N. J.; Zhu, Z.; Amal, R.; Smith, S. C. Hybrid Graphene/Titania Nanocomposite: Interface Charge Transfer, Hole Doping, and Sensitization for Visible Light Response. *J. Phys. Chem. Lett.* **2011**, *2*, 894−899.
(32) Li, X.; Gao, H.; Liu, G. A LDA+U Study of the Hybrid Graphene/Anatase TiO_2 Nanocomposites: Interfacial Properties and Visible Light Response. *Comput. Theor. Chem.* **2013**, *1025*, 30−34.
(33) Long, R. Electronic Structure of Semiconducting and Metallic Tubes in TiO_2/Carbon Nanotube Heterojunctions: Density Functional Theory Calculations. *J. Phys. Chem. Lett.* **2013**, *4*, 1340−1346.
(34) Long, R.; Dai, Y.; Huang, B. Fullerene Interfaced with a TiO_2(110) Surface May Not Form an Efficient Photovoltaic Heterojunction: First-Principles Investigation of Electronic Structures. *J. Phys. Chem. Lett.* **2013**, *4*, 2223−2229.
(35) Xu, L.; Huang, W.-Q.; Wang, L.-L.; Huang, G.-F.; Peng, P. Mechanism of Superior Visible-Light Photocatalytic Activity and Stability of Hybrid Ag_3PO_4/Graphene Nanocomposite. *J. Phys. Chem. C* **2014**, *118*, 12972−12979.
(36) Geng, W.; Zhao, X.; Liu, H.; Yao, X. Influence of Interface Structure on the Properties of ZnO/Graphene Composites: a Theoretical Study by Density Functional Theory Calculations. *J. Phys. Chem. C* **2013**, *117*, 10536−10544.
(37) Xu, P.; Tang, Q.; Zhou, Z. Structural and Electronic Properties of Graphene-ZnO Interfaces: Dispersion-Corrected Density Functional Theory Investigations. *Nanotechnology* **2013**, *24*, 305401.
(38) Dresselhaus, M.; Thomas, I. Alternative Energy Technologies. *Nature* **2001**, *414*, 332−337.
(39) Trovarelli, A.; Fornasiero, P. *Catalysis by Ceria and Related Materials*, 2nd ed.; Imperial College Press: London, 2013.
(40) Wang, G.; Bai, J.; Wang, Y.; Ren, Z.; Bai, J. Prepartion and Electrochemical Performance of a Cerium Oxide−Graphene Nanocomposite as the Anode Material of a Lithium Ion Battery. *Scr. Mater.* **2011**, *65*, 339−342.
(41) Wang, Y.; Guo, C. X.; Liu, J.; Chen, T.; Yang, H.; Li, C. M. CeO_2 Nanoparticles/Graphene Nanocomposite-Based High Performance Supercapacitor. *Dalton Trans.* **2011**, *40*, 6388−6391.
(42) da Silva, M.; de Jesus Fraga da Costa, H.; Triboni, E.; Politi, M.; Isolani, P. Synthesis and Characterization of CeO_2−Graphene Composite. *J. Therm. Anal. Calorim.* **2012**, *107*, 257−263.
(43) Jiang, L.; Yao, M.; Liu, B.; Li, Q.; Liu, R.; Lv, H.; Lu, S.; Gong, C.; Zou, B.; Cui, T.; Liu, B. Controlled Synthesis of CeO_2/Graphene Nanocomposites with Highly Enhanced Optical and Catalytic Properties. *J. Phys. Chem. C* **2012**, *116*, 11741−11745.
(44) Wang, X.; Li, X.; Liu, D.; Song, S.; Zhang, H. Green Synthesis of Pt/CeO_2/Graphene Hybrid Nanomaterials with Remarkably Enhanced Electrocatalytic Properties. *Chem. Commun.* **2012**, *48*, 2885−2887.
(45) Jiang, L.; Yao, M.; Liu, B.; Li, Q.; Liu, R.; Yao, Z.; Lu, S.; Cui, W.; Hua, X.; Zou, B.; Cui, T.; Liu, B. Shape-Selective Synthesis and Optical Performance of Ceria Nanocrystal/Graphene Hybrid Composites. *CrystEngComm* **2013**, *15*, 3739−3743.
(46) Ling, Q.; Yang, M.; Rao, R.; Yang, H.; Zhang, Q.; Liu, H.; Zhang, A. Simple Synthesis of Layered CeO_2−Graphene Hybrid and Their Superior Catalytic Performance in Dehydrogenation of Ethylbenzene. *Appl. Surf. Sci.* **2013**, *274*, 131−137.
(47) Srivastava, M.; Das, A. K.; Khanra, P.; Kim, N. H.; Lee, J. H. A Facile One-Step Hydrothermal Synthesis of Graphene/CeO_2 Nanocomposite and its Catalytic Properties. *Adv. Mater. Res.* **2013**, *747*, 242−245.
(48) Su, Q.; Chang, L.; Zhang, J.; Du, G.; Xu, B. In Situ TEM Observation of the Electrochemical Process of Individual CeO_2/Graphene Anode for Lithium Ion Battery. *J. Phys. Chem. C* **2013**, *117*, 4292−4298.
(49) Ji, Z.; Shen, X.; Li, M.; Zhou, H.; Zhu, G.; Chen, K. Synthesis of Reduced Graphene Oxide/CeO_2 Nanocomposites and Their Photocatalytic Properties. *Nanotechnology* **2013**, *24*, 115603.
(50) Huang, K.; Li, Y.; Lin, S.; Liang, C.; Xu, X.; Zhou, Y.; Fan, D.; Yang, H.; Lang, P.; Zhang, R.; Wang, Y.; Lei, M. One-Step Synthesis of Reduced Graphene Oxide−CeO_2 Nanocubes Composites with Enhanced Photocatalytic Activity. *Mater. Lett.* **2014**, *124*, 223−226.
(51) Shailendra, K. J.; Naveen Kumar, C.; Pavul Raj, R.; Niki, S. J.; Mohan, S. Synthesis of 3D Porous CeO_2/reduced Graphene Oxide Xerogel Composite and Low Level Detection of H_2O_2. *Electrochim. Acta* **2013**, *120*, 308−313.
(52) Ji, Z.; Shen, X.; Yang, J.; Zhu, G.; Chen, K. A Novel Reduced Graphene Oxide/Ag/CeO_2 Ternary Nanocomposite: Green Synthesis and Catalytic Properties. *Appl. Catal., B* **2014**, *144*, 454−461.
(53) Kresse, G.; Furthmüller, J. Efficient Iterative Schemes for Ab Initio Total-Energy Calculations Using a Plane-Wave Basis Set. *Phys. Rev. B* **1996**, *54*, 11169.
(54) Kresse, G.; Furthmüller, J. Efficiency of Ab Initio Total Energy Calculations for Metals and Semiconductors Using a Plane-Wave Basis Set. *Comput. Mater. Sci.* **1996**, *6*, 15−50.
(55) Blöchl, P. E. Projector Augmented-Wave Method. *Phys. Rev. B* **1994**, *50*, 17953.
(56) Ceperley, D. M.; Alder, B. Ground State of the Electron Gas by a Stochastic Method. *Phys. Rev. Lett.* **1980**, *45*, 566.
(57) Monkhorst, H. J.; Pack, J. D. Special Points for Brillouin-Zone Integrations. *Phys. Rev. B* **1976**, *13*, 5188.
(58) Ramasubramaniam, A. Electronic Structure of Oxygen-Terminated Zigzag Graphene Nanoribbons: A Hybrid Density Functional Theory Study. *Phys. Rev. B* **2010**, *81*, 245413.
(59) Hay, P. J.; Martin, R. L.; Uddin, J.; Scuseria, G. E. Theoretical Study of CeO_2 and Ce_2O_3 Using a Screened Hybrid Density Functional. *J. Chem. Phys.* **2006**, *125*, 034712.
(60) Da Silva, J. L. F.; Ganduglia-Pirovano, M. V.; Sauer, J.; Bayer, V.; Kresse, G. Hybrid Functionals Applied to Rare-Earth Oxides: The Example of Ceria. *Phys. Rev. B* **2007**, *75*, 045121.
(61) Désaunay, T.; Ringuedé, A.; Cassir, M.; Labat, F.; Adamo, C. Modeling Basic Components of Solid Oxide Fuel Cells Using Density Functional Theory: Bulk and Surface Properties of CeO_2. *Surf. Sci.* **2012**, *606*, 305−311.
(62) Srivastava, M.; Das, A. K.; Khanra, P.; Uddin, M. E.; Kim, N. H.; Lee, J. H. Characterizations of in Situ Grown Ceria Nanoparticles on Reduced Graphene Oxide as a Catalyst for the Electrooxidation of Hydrazine. *J. Mater. Chem. A* **2013**, *1*, 9792−9801.
(63) Huang, K.; Lei, M.; Wang, Y.; Liang, C.; Ye, C.; Zhao, X.; Li, Y.; Zhang, R.; Fan, D.; Wang, Y. Green Hydrothermal Synthesis of CeO_2 NWs−Reduced Graphene Oxide Hybrid with Enhanced Photocatalytic Activity. *Powder Diffr.* **2014**, *29*, 8−13.
(64) Pfeifer, V.; Erhart, P.; Li, S.; Rachut, K.; Morasch, J.; Brotz, J.; Reckers, P.; Mayer, T.; Ruhle, S.; Zaban, A. Energy Band Alignment between Anatase and Rutile TiO_2. *J. Phys. Chem. Lett.* **2013**, *4*, 4182−4187.
(65) Meyer, J. C.; Geim, A. K.; Katsnelson, M.; Novoselov, K.; Booth, T.; Roth, S. The Structure of Suspended Graphene Sheets. *Nature* **2007**, *446*, 60−63.
(66) Kamat, P. V. Manipulation of Charge Transfer Across Semiconductor Interface. A Criterion that Cannot be Ignored in Photocatalyst Design. *J. Phys. Chem. Lett.* **2012**, *3*, 663−672.
(67) Long, R.; English, N. J.; Prezhdo, O. V. Photo-Induced Charge Separation across the Graphene−TiO_2 Interface Is Faster than Energy Losses: A Time-Domain Ab Initio Analysis. *J. Am. Chem. Soc.* **2012**, *134*, 14238−14248.
(68) Duncan, W. R.; Prezhdo, O. V. Theoretical Studies of Photoinduced Electron Transfer in Dye-Sensitized TiO_2. *Annu. Rev. Phys. Chem.* **2007**, *58*, 143−184.
(69) Tafen, D. N.; Long, R.; Prezhdo, O. V. Dimensionality of Nanoscale TiO_2 Determines the Mechanism of Photoinduced Electron Injection from a CdSe Nanoparticle. *Nano Lett.* **2014**, *14*, 1790−1796.